



CHORUS

This is the accepted manuscript made available via CHORUS. The article has been published as:

Experimental study of the valence band of $\text{Bi}_{\{2\}}\text{Se}_{\{3\}}$

Yi-Bin Gao (□□□), Bin He, David Parker, Ioannis Androulakis, and Joseph P. Heremans

Phys. Rev. B **90**, 125204 — Published 26 September 2014

DOI: [10.1103/PhysRevB.90.125204](https://doi.org/10.1103/PhysRevB.90.125204)

Experimental study of the valence band of Bi_2Se_3

Yi-Bin Gao (高亦斌)¹, Bin He¹, David Parker², Ioannis Androulakis³ and Joseph P. Heremans^{1, 4,*}

1. Department of Mechanical and Aerospace Engineering, The Ohio State University, Columbus, Ohio 43210
2. Materials Science and Technology Division, Oak Ridge National Laboratory, Oak Ridge, TN 37831
3. Gentherm Inc., 1321 Mountain View Circle, Azusa, CA 91702
4. Department of Physics, The Ohio State University, Columbus, Ohio 43210

Abstract

The valence band of Bi_2Se_3 is investigated by measuring Shubnikov-de Haas effect as well as galvanomagnetic and thermoelectric transport. At low hole concentration, the hole Fermi surface is closed and box-like, but at higher carrier concentrations it develops tube-like extensions that are open, in general agreement with our theoretical calculations. However, the experimentally determined density-of-states effective mass is smaller than density-functional theory calculations predict; while we cannot give a definitive explanation for this, we suspect that the theory may lack sufficient precision to compute room-temperature transport properties, such as the thermopower, in solids with interlayer Van der Waals bonds.

I. Introduction

Bi_2Se_3 has the same $\bar{3}m$ crystal structure as Bi_2Te_3 , the thermoelectric semiconductor that is at the basis of commercial Peltier coolers. Bi_2Se_3 and Bi_2Te_3 form solid solutions¹, and the optimization studies² aimed at obtaining high thermoelectric figure-of-merit (zT) values in the $\text{Bi}_2\text{Te}_x\text{Se}_{3-x}$ alloy system have been focused on the Te-rich ($x \geq 1.5$) region. Where Bi_2Te_3 can be easily doped either p-type or n-type, the defect chemistry of Bi_2Se_3 is such that material prepared at thermodynamic equilibrium is always n-type.^{3,4} The only report⁵ on p-type Bi_2Se_3 before this decade has not been repeated. The nature of native defects in Bi_2Se_3 is still an open debate; there are two opinions: Analytis et al.⁶ argue that the defects are Se vacancies, while Huang et al.⁷ claim that there are Bi_{Se} anti-site defects and additional layers. The band structure features and strong spin-orbit interactions of Bi_2Se_3 are favorable for the development of topologically protected surface states, which has been the basis behind recent efforts to make intrinsic and/or doped p-type Bi_2Se_3 . Several new acceptor impurities have been discovered for Bi_2Se_3 , including Ca,⁸ Mn,⁹ Mg,¹⁰ and Pb (this work). Yet, it is suspected that the native defects of Bi_2Se_3 still exist even in the presence of these chemical acceptors, and we do not know if the p-type material is compensated, or if the acceptor impurities alleviate the donor action of the native defects.

It was recently predicted by calculation that the valence band of Bi_2Se_3 could be favorable to produce a high-zT thermoelectric material.¹¹ The existence of high-mobility p-type Bi_2Se_3 now makes it possible to study the valence band of p-type Bi_2Se_3 experimentally, and to compare the results with the calculations. The electronic band structure of Bi_2Se_3 is very

different from Bi_2Te_3 , which has 6-fold band degeneracy (equivalent bands in Brillouin zone) near the band gap and the Fermi level, whereas Bi_2Se_3 has only one in the center (Γ point) of the Brillouin zone. Higher band degeneracy improves zT because it increases density of states effective mass, which allows the material to have a higher carrier concentration and therefore better electrical conductivity without affecting the thermopower. The conduction band of Bi_2Se_3 has a low effective mass ($\sim 0.21 m_e$, where m_e is the free electron mass^{3,4}), therefore is a poor candidate material for high zT . The valence band, however, is more complex.¹¹ We show in Fig. 1 the hole Fermi surface (generated from data in Ref [11] using code in Ref [12]) for hole concentrations of $6 \times 10^{18} \text{cm}^{-3}$ and $4 \times 10^{19} \text{cm}^{-3}$ respectively. The Fermi surface in Fig. 1(a) has a “bag”-shape pocket centered around Γ -point. In Fig.1 (b) there are six additional topologically open pieces, “pipes”, which connect to the adjacent Brillouin zones. At lower carrier concentrations, the pipes separate from the bag. The bag now becomes a topologically closed surface, and the pipes transform into small, ellipsoidal, and separated pockets that are also topologically closed. At lower concentrations still, only the central bag remains.

The purpose of the present paper is to show these features experimentally using Shubnikov-de Haas (SdH) band structure measurements on a series of single crystal samples with different doping levels. From a Dingle analysis of the data¹³ we derive values for the cyclotron effective mass, which are at odds with the calculated¹¹ values. We complement the SdH experiment with a series of transport measurements made on polycrystalline samples prepared with different acceptor impurities and different doping levels. Measurements of the Hall effect and thermopower are used to construct the hole concentration dependence of the thermopower (the “Pisarenko” plot). This can give an estimate of the density-of-states

effective mass. While the density of states mass and the cyclotron mass are not the same, the relatively cubic shape of the “bag” in Fig. 1 (a) shows that they are not expected to differ by much. Experimentally, the value of the valence band effective mass obtained from the Pisarenko plot is consistent with that obtained from SdH measurements. The valence band mass is only about 20% heavier than the conduction band mass,^{3,4} and significantly smaller than predicted by the calculations.¹¹ A first conclusion of this paper is that p-type Bi_2Se_3 is not likely to be a significantly better thermoelectric semiconductor than any n-type variant of this material. This paper further concludes by presenting a rationale for the discrepancy in calculated properties¹¹ and the experimental measurements, and then suggest a more fundamental explanation related to the presence of Van der Waals interlayer bonds in Bi_2Se_3 material. The density functional theory used in Ref [11] is less accurate in solids with such weak bonding, and in fact the development of new Van der Waals energy functionals is an active and ongoing area of research.¹⁴ This second conclusion is likely to have implications for band structure calculations of many of today’s bulk 2-dimensional-like solids.

II. Experiment

We prepared a series of 4 single crystals and 6 polycrystalline samples: sample identification and properties are summarized in Table 1. For the single crystals, 99.999% pure Bi and Se were weighted into quartz ampoules and acceptor impurities Ca or Mn and were added in appropriate amounts to dope Bi_2Se_3 p-type. The ampoules were evacuated to 10^{-6} Torr, sealed, and the elements were then melted and reacted at 1073 K. Single crystals of Bi_2Se_3 were grown by slow cooling using a modified horizontal Bridgman method described in Ref [8]. The single crystals cleave easily perpendicularly to the c axis. We limit our discussion to self-consistent

data on small individual cleaved samples with a characteristic size of 0.2mm×1mm×4mm, in which we were able to confirm sufficient homogeneity via the presence of quantum oscillations in the resistivity measurements. The polycrystalline samples were prepared by ball milling and spark plasma sintering. Stoichiometric and off-stoichiometric Bi₂Se₃ doped with Mg or Mn (see Table 1 for detail) were weighted and loaded into a quartz ampoule. The ampoule was evacuated to 10⁻⁶ Torr, sealed, and then heated to 1073K where it was kept overnight to ensure homogeneity. The furnace was turned off and the ingot was allowed to gradually cool to room temperature. The sample was removed from the ampoule and ground by hand. The resulting powder was then formed into a pellet by Spark Plasma Sintering (SPS) at 623K under 50MP of pressure. The sintered pellet was cut into a 6mm×2mm×2mm rectangular parallelepiped for transport measurements. The electrical and thermal properties of the disks cannot be expected to be isotropic, since the process favors the alignment of the c-axis of the Bi₂Se₃ polycrystals with the pressing direction. To account for this, small parallelepipeds were cut out, and the thermopower and Hall coefficients were measured with the heat and charge currents in the plane of the pressing, i.e. preferentially aligned in the basal plane of the crystallites.

The resistivity, ρ , and low-field Hall coefficient, R_H , of the single crystals were measured in a Quantum Design PPMS from 2K to 300K. Shubnikov-de Haas (SdH) oscillations were measured in the same instrument on the same sample from 2K to 12K in magnetic fields up to 140 kOe. The cleaved single crystal samples were mounted on a horizontal rotator, and the angular dependence of the SdH oscillations was measured by varying the orientation of the sample relative to the applied magnetic field (the elevation angle, set at $\pi/2$ when the applied field is aligned with the trigonal axis). No attempt was made to align the electrical current with

the azimuthal angle in the basal plane. The thermopower S and the Hall coefficient of the polycrystalline samples were measured in a Janis cryostat from 77K to 300K in magnetic fields up to 13 kOe.

III. Results

The hole concentration, p , is obtained using $p = 1/(R_H e)$, where e is the elementary charge, assuming that the Hall prefactor is unity. The hole concentrations of the single crystals are shown in Fig. 2(a). Temperature dependence of thermopower is measured on the same samples and shown in Fig. 2(b). The Drude mobility is calculated using $\mu = R_H / \rho$ and shown in Fig. 2(c), while the temperature dependence of resistivity is shown in Fig. 2(d). All of the samples show metallic behavior, with the carrier concentration being temperature independent from 2K to 200K and varying little with temperature above that. Some of this temperature variation may be due to variation of the Hall prefactor. The hole concentrations (Table 1) were calculated from the low-temperature ($T \leq 100$ K) value of R_H . The mobility decreases monotonically with temperature, indicating that the charge carriers are scattered predominantly by phonons. The measured carrier concentrations and the mobilities both have an error bar of 5%, mostly from sample geometry measurement (error bars are not shown in the figures to improve readability). The p-type Bi_2Se_3 single crystals have a room temperature mobility $\sim 500 \text{ cm}^2\text{V}^{-1}\text{s}^{-1}$, less than the electron mobilities in typical n-type Bi_2Se_3 single crystals, which can reach above $1000 \text{ cm}^2\text{V}^{-1}\text{s}^{-1}$ around room temperature.

Raw traces of the SdH oscillations observed in the resistivity as a function of elevation angle on the samples S1-S4 are shown in Fig. 3: the main period as function of the inverse of

the field is obvious and periodic, and Fourier transforms of these traces have been determined. The accuracy (std. dev.) on the main oscillation period is ~3%. Other minor peaks also appear in the Fourier transforms, but they are likely to be artifacts, as they are not robust enough vis-à-vis changes in the numerical treatment to be identified as real SdH periods: in the analysis we consider only the main period, which is the one visible to the naked eye in Fig. 3. The cross-section of the Fermi surface, a_F , in the plane normal to the applied magnetic field can be directly calculated from the period of the oscillation¹³ by the following equation:

$$a_F = \frac{2\pi e}{\hbar \Delta [1/B]}. \quad (1)$$

We identify the main period to be associated with the Fermi surface centered at Γ point in Fig. 1. Polar plots of the periods $\{\Delta [1/B]\}^{-1}$ as a function of elevation angle are shown for all samples (identified by their hole concentration as measured by the Hall effect) in Fig. 4. The polar plots show how the Fermi surface cross-sectional area increases with increasing carrier concentration. Anomalies in cross-sectional area appear in the more highly doped samples in the vicinity of 105 deg, which we associate with appearance of the open orbits, as illustrated in Fig. 1(b).

We now discuss the comparison between the shapes and sizes of the Fermi surfaces as calculated (Fig. 1) and the cross-section measured in Fig. 4. Starting with sample S1, and using the crude assumption that the Fermi surface is spherical at this concentration, the SdH oscillations period at 0 deg (950 kG) would correspond to a hole concentration of $5.2 \times 10^{18} \text{ cm}^{-3}$, while and the period at 90deg (1220 kG) corresponds to $7.6 \times 10^{18} \text{ cm}^{-3}$. These values bracket the measured hole concentration obtained from Hall measurements of $5.7 \times 10^{18} \text{ cm}^{-3}$: it is thus

reasonable to conclude that the holes occupy a Fermi surface with relatively little anisotropy, which is most likely the central “bag” at the Γ point in Fig. 1(a). Additional bands are not expected at this concentration, and are indeed not seen.

Sample S2 ($1.4 \times 10^{19} \text{ cm}^{-3}$ holes) shows a bump at a 120 deg angle, which indicates the onset of an extension of the “bag-shaped” Fermi surface in that direction and the beginning of the formation of the “pipe-like” structures. Applying the same spherical Fermi surface approximation used above to sample S2 (which is a clearly unrealistic model for describing the behavior of this sample), the corresponding oscillation period at 0 deg (123 kOe) would yield $p = 7.7 \times 10^{18} \text{ cm}^{-3}$. In reality, the Hall measurement gives $1.4 \times 10^{19} \text{ cm}^{-3}$. While Hall measurements are less accurate than SdH measurements because they involve a measurement of the sample geometry and an assumption about the Hall prefactor, we conclude from this discrepancy that the shape of the Fermi surface must deviate considerably from spherical. This behavior becomes even more pronounced in samples S3 and S4, where the oscillation period disappears completely near 105 deg. This, in turn, implies that the cross-section of Fermi surface normal to that direction is open: it reaches the boundary of the first Brillouin zone and connects to the Fermi surface of the next Brillouin zone, such that the carrier orbits encompass all Brillouin zones and the holes never complete a cyclotron orbit.

SdH measurements also make it possible to measure the holes’ cyclotron effective mass by the Dingle analysis method,¹³ based on the temperature dependence of the amplitude of the SdH oscillation. The amplitude of the SdH oscillation is reduced by a reduction factor, R_T , given

as a function of the average carrier effective cyclotron mass, m^* , on the orbit and applied magnetic field H :¹³

$$R_T = \frac{147 \frac{m^*}{m_e} \frac{T(K)}{H(kOe)}}{\sinh \left\{ 147 \frac{m^*}{m_e} \frac{T(K)}{H(kOe)} \right\}}, \quad (2)$$

where m_e is the free electron mass. This analysis is carried out for each sample, at multiple values of the field and the temperature, using two fitting parameters: the cyclotron mass m^* and the Dingle temperature, which is a function of the sample defect density. Fig. 5 illustrates how all T-dependences of the amplitudes taken at various values of the applied field aligned along the c-axis (normalized to the value at 2K and 1.36×10^6 G) fit Eq. (2) well for one single value for all samples of the valence band effective mass $m^* = 0.25 \pm 0.05 m_e$. Furthermore, values for the average in-plane effective mass are the same for all 4 samples of different carrier concentrations, and for those doped with two different acceptor impurities (Ca and Mn). The Dingle temperatures do vary from sample to sample (30 K for the Mn-doped sample, 9 – 17 K for the Ca-doped ones), but yield no information beyond the observation that Mn doping affects the phase coherence length of the electrons on Landau levels more than Ca-doping, presumably because of the d-electrons in Mn^{2+} .

To verify this value for m^* independently, we prepared the polycrystalline samples and measured their hole concentration, p , and thermopower, S , in order to construct the Pisarenko plot $S(p)$. This plot gives an independent evaluation of the experimental effective mass, albeit one that depends on an assumption about electron scattering. The results, taken on samples

P1-P6, are shown in Fig. 6, in which the data are shown as points, and calculated curves as lines. The calculations must assume a value for the energy dependence of the relaxation time, which is customarily taken as a power law $\tau(E) = \tau_0 E^\lambda$, with λ being the scattering parameter. Schematically, $\lambda=-1/2$ is indicative of carrier scattering on acoustic phonons, $\lambda=1/2$ of scattering on polar optical phonons, and $\lambda=3/2$ of scattering on ionized impurities, such as acceptor impurities. Because the latter is mostly a low-temperature effect, we show a few possibilities in Fig. 6: $m^* = 0.25 m_e$ with $\lambda=-1/2$ and $\lambda=1/2$, and $m^* = 0.4 m_e$ with $\lambda=-1/2$. The samples with $p < 10^{19} \text{ cm}^{-3}$ fall on the lowest curve ($m^* = 0.25 m_e$ with $\lambda=-1/2$), which is consistent with the mass from the SdH data. Some deviation is observed for $p > 10^{19} \text{ cm}^{-3}$, but it is not large enough to explain the discrepancy between theory and experiment described underneath. It is also not possible to ascertain whether this is due to an increase in effective mass or a change in scattering mechanism. Moreover, the SdH mass reported here is average cyclotron mass in the basal plane, whereas the Pisarenko plot measures the total density-of-states mass; those two quantities are equal only for a spherical Fermi surface, but, as discussed above, the “bag” in the Fermi surface does not depart appreciable from spherical. Fig. 4 shows that the hole Fermi surface departs only slightly from spherical when $p \leq 6 \times 10^{18} \text{ cm}^{-3}$, so that the fact that a mass of $0.25 m_e$ explains the $S(p)$ results well in that concentration range shows that transport and SdH results are consistent. When the carrier concentration reaches above about $1.4 \times 10^{19} \text{ cm}^{-3}$, the Fermi surface deviates from spherical and the average DOS mass increases above the basal-plane cyclotron mass. This is again also consistent with the results in Fig. 6 at higher hole concentrations. Nevertheless, the main conclusion holds: all the experimental $S(p)$ data points in Fig. 6 are significantly below the theoretical calculated values of Ref. [11], but are compatible

with the values for the effective mass observed in the SdH measurements. This independently confirms the already mentioned discrepancy between calculated and measured effective masses. The difference in the experimental result and the theoretical calculation is shown in Fig. 7. Similar results were also reported by Cava's group⁹.

IV. Theoretical Calculations and Discrepancy with Experimental Data

The Fermi surface plot presented in Fig. 1 was derived from well-converged band structure calculations, as described in Ref. [11]. These calculations were performed using the plane-wave code WIEN2K¹⁵ within the generalized gradient approximation of Perdew et al.,¹⁶ with spin-orbit coupling included for all calculations excepting the internal coordinate optimization. The Fermi surface plot is based on a very dense k-point mesh of approximately 75,000 points in the full rhombohedral Brillouin zone. In addition, effective planar cyclotron masses were generated from the band structure calculations using the program SKEAF¹⁷ at various doping levels: these are presented as lines in Fig. 7, where they are compared to the experimental masses from the Dingle analysis of the SdH oscillations above. The effective masses vary somewhat with doping level, and are comprised of two main sequences. The first, heavier mass is in the range of $m_H^* \sim 0.4 - 0.6 m_e$ and corresponds to the central "bag" feature, while the lighter mass of $m_L^* \sim 0.15 - 0.17 m_e$ corresponds to the "pipe" feature. Note that the "pipe" mass is not shown for doping levels less than 1.44×10^{-3} holes per unit cell, as at this doping any "pipe" features are beyond the resolution of our calculations. In any case, as was noted earlier in this manuscript, the observed masses, even excluding entirely the "pipe" features, are considerably larger than those inferred from the experimental data, and it is this

discrepancy in effective masses that appears to be responsible for the lower thermopower in the experiment relative to the theoretical predictions in Ref. [11]. Note that an earlier paper from the Cava group (Ref. [9]) also showed thermopower smaller than the predictions of Ref. [11]. Therefore, it appears likely that the theoretical calculation does not accurately represent the valence band effective mass, and consequently the room temperature Seebeck coefficient. Since the calculation and even prediction of thermopower levels is a subject of substantial interest to the thermoelectrics community, with numerous recent successes in PbSe¹⁸ and SnTe¹⁹, it is important to attempt to determine the origin of the discrepancy between theory and experiment.

One possibility that can be immediately discarded is the use of the “constant scattering time approximation” in the Boltzmann transport calculation²⁰ of the thermopower, because the masses derived here come from quantum oscillations, and not just from Pisarenko relations. The discrepancy in effective masses, entirely sufficient to explain the thermopower differences, is a comparison of ground state properties completely unrelated to any assumptions made regarding the diffusive carrier transport.

While it is not possible to state with confidence the reason for the discrepancy, we can hazard a possible explanation. Consider the three plots taken from literature calculations in references [11], [21] and [22] of the band structure of Bi₂Se₃. At first sight, they appear fairly similar in their appearance, but a closer examination reveals important differences. For example, in the plot in Ref. [22] the valence band maximum is not at Γ as in the other two plots, but rather at an off-symmetry location. While the other two plots have a subsidiary valence-

band extremum at this same location, even these two differ as to the precise location of the extremum, with the top plot placing this extremum just 30 meV from the band edge and the middle plot approximately 85 meV from the band edge. Note that in the bottom plot this extremum *is* the band edge. Given that the thermopower data presented in this paper were measured at room temperature, for which the thermal energy $k_B T$ is just 25 meV, a 55 meV difference in the location of a subsidiary band extremum would have substantial effects on transport properties. Another area of disagreement is the location in energy of the valence band Z point, where the respective values are (from Ref. 11, 21 and 22, in order) -0.25 eV, -0.6 eV, and -0.5 eV.

With regards to calculated dispersions and band masses, in Table 2 we present Γ -Z-point valence band masses inferred from the calculations published in Refs. [9,19,20,24]. Note that for two of these calculations – the work of Zhang et al Ref. [22] and Larson et al Ref. [24] – the Γ point is not calculated to be the valence band maximum, contrary to present experimental fact, but we present the results for purposes of illustration.

The calculated results depict a wide disparity in masses, with as much as a factor of 6 separating the heaviest and lightest masses. These masses were calculated by assuming a Γ -centered parabolic band dispersion and using a point halfway from Γ to Z as the dispersion, so some variance with values presented elsewhere in this report is inevitable. Nevertheless, the wide ranges in values calculated is strong evidence of the challenge to electronic structure calculations posed by the valence band of Bi_2Se_3 .

Given that published band structure calculations disagree on such fundamental matters as the location of the VBM, and the energies of subsidiary band extrema, as well as band masses, it appears that Bi_2Se_3 is an unexpectedly difficult material in which to accurately depict the detailed electronic structure. For transport properties and SdH in the temperature range of 2K to 300K, these features are of great importance. While one cannot give a definitive explanation for the disagreements, we suggest that the answer may lie in the status of Bi_2Se_3 as a Van der Waals bonded material (for interlayer bonding). Such weak bonding presents density functional theory with more difficulties than with more ionic or covalently bonded materials, and in fact the development of new Van der Waals energy functionals is an active area of research.²³ We think it plausible, though unproven, that such is the origin of the discrepancies between theory and experiment identified in the present work.

V. **Summary and Conclusion**

In summary, we observe that the value of the density-of-states effective mass for the valence band of Bi_2Se_3 is significantly smaller than had been theoretically predicted. This in turn affects the calculated theoretical thermopower. From this, we conclude that the prospects of p-type Bi_2Se_3 as a thermoelectric material are not as promising as originally predicted, and that density functionals may need to be critically evaluated before use in band structure calculations for room temperature transport properties in solids with Van der Waals bonds.

Acknowledgements

This work is supported by NSF grant CBET-1048622, by Gentherm Inc. (www.gentherm.com), and (D.P.) by the Department of Energy, Basic Energy Sciences, through the S3TEC Energy

Frontier Research Center. Y-B Gao thanks Richard L. J. Qiu and Michele D. Nielsen for helpful discussions.

Tables

Sample No	Nominal composition	Hole concentration (10^{18} cm^{-3})	Thermopower @300K ($\mu\text{V/K}$)	Symbol in this paper
S1	$\text{Bi}_{1.97}\text{Mn}_{0.03}\text{Se}_3$	5.7@100K	146	
S2	$\text{Bi}_{1.95}\text{Ca}_{0.05}\text{Se}_{2.975}$	14@100K	140	
S3	$\text{Bi}_{1.98}\text{Ca}_{0.02}\text{Se}_{3.03}$	14@100K	144	
S4	$\text{Bi}_{1.99}\text{Ca}_{0.01}\text{Se}_{3.03}$	16@100K	134	
P1	$\text{Bi}_{1.98}\text{Pb}_{0.02}\text{Se}_{3.01}$	9.3@100K	109	
P2	$\text{Bi}_{1.96}\text{Pb}_{0.04}\text{Se}_{3.01}$	9.8@100K	93	
P3	$\text{Bi}_{1.96}\text{Mg}_{0.02}\text{Se}_3$	8.5@100K	131	
P4	$\text{Bi}_{1.99}\text{Mg}_{0.01}\text{Se}_{3.06}$	13@300K	131	
P5	$\text{Bi}_{1.98}\text{Mg}_{0.02}\text{Se}_{3.03}$	14@100K	114	
P6	$\text{Bi}_{1.96}\text{Mg}_{0.04}\text{Se}_{3.06}$	18@300K	116	

Table 1 Summary of the samples used in this study. Sample numbers starting with S identify single crystals, and P for polycrystals. The acceptor impurities used, Mn, Ca, Pb or Mg, are shown in the nominal composition. The hole concentrations are derived from Hall effect measurements at 100 K. The symbols in the last column are consistent with the figures throughout this article.

Publication	Calculated mass (units of m_0)
Mishra et al [21]	0.36
Parker et al [11]	0.80
Zhang et al [22]	2.20
Larson et al [24]	0.56

Table 2: Calculated Bi_2Se_3 valence band masses for the Γ -Z direction

Figure Captions

Fig. 1 (color online) Calculated hole Fermi surface of Bi_2Se_3 at hole concentration of $6 \times 10^{18} \text{cm}^{-3}$ (top) and $4 \times 10^{19} \text{cm}^{-3}$ (bottom), using the methods developed in Ref [11], (a) has the “bag” region whereas (b) has both “bag” and “pipes” region. The pipes are connected to the adjacent Brillouin zones.

Fig. 2 (color online) Experimental temperature dependence of (a) the carrier concentration as measured by Hall effect, (b) the thermopower, (b) the mobility, and (c) the resistivity of the single-crystal p-type Bi_2Se_3 samples studied here. The insert in (a) shows the field-dependence at 10 K of the Hall resistivity, illustrating a simple linear relation indicative of single-band conduction.

Fig. 3 (color online) Angular dependence of Shubnikov – de Haas oscillations trace for all single crystal sample measured. The angle is elevation angle between the direction of applied magnet field and the basal plane: (1) 0° (2) 30° (3) 60° (4) 90° (5) 120° (6) 150° (7) 180° . The frames (a)-(d) are for samples S1-S4 (see Table 1).

Fig. 4 (color online) Polar plot of the cross-sectional area of the Fermi surface, as a function of the elevation angle from the basal plane (0°) toward the c-axis (90°). The plots are shown for different doping levels, as indicated.

Fig. 5 (color online) Characteristic temperature dependence of SdH oscillation amplitude. The symbols are the experimental data points, plotted for different values of the magnetic field as

indicated. All solid lines are fits to Eq. (2) with a single parameter, an effective mass $m^* = 0.25m_e$. The Dingle temperatures vary from sample to sample.

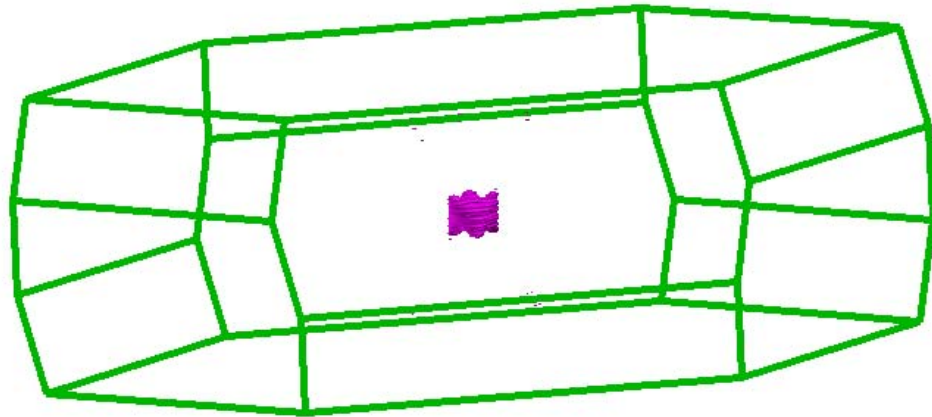
Fig. 6 (color online) Thermopower at 300 K versus hole concentration as measured by the Hall effect at 100 K, for p-type Bi_2Se_3 , following the symbol and color conventions given in Table 1

Fig. 7 (color online) Measured (data points) and calculated (lines) density-of-states hole effective mass vs. doping level. The heavy hole mass m_H^* corresponds to the central “bag” in the Fermi surface shown in Fig. 1, the light mass m_L^* to the “pipes”, as illustrated in Fig. 1.

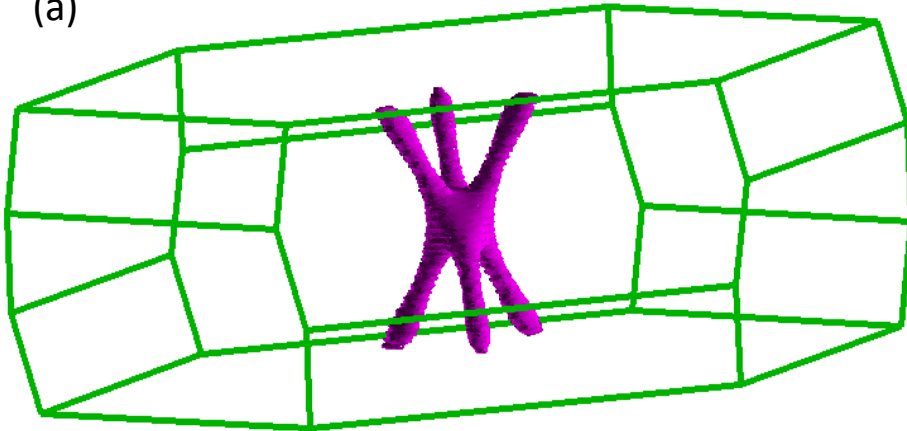
References

-
- ¹ S. Nakajima, J. Phys. Chem. Solids. **24**, 479 (1963)
- ² H. Scherrer and S. Scherrer, *CRC Handbook of Thermoelectrics*, D. M. Rowe, Editor, pp. 211-237. CRC Press, Inc., 1994.
- ³ H. Köhler, Solid State Commun. **13**, 1585 (1973)
- ⁴ H. Köhler and A. Fabbicius, Phys. Status Solidi B. **71**, 487 (1975)
- ⁵ J.A. Woollam, H. Beale, and I.L. Spain, Phys. Lett. A **41**, 319 (1972)
- ⁶ J.G. Analytis, Jiun-Haw Chu, Yulin Chen, Felipe Corredor, Ross D. McDonald, Z. X. Shen, and Ian R. Fisher, Phys. Rev. B **81**, 205407 (2010).
- ⁷ F.-T. Huang, M.-W. Chu, H. H. Kung, W. L. Lee, R. Sankar, S.-C. Liou, K. K. Wu, Y. K. Kuo, and F. C. Chou, Phys. Rev. B **86**, 081104 (2012)
- ⁸ Y.S. Hor, A. Richardella, P. Roushan, Y. Xia, J. G. Checkelsky, A. Yazdani, M. Z. Hasan, N. P. Ong, and R. J. Cava, Phys. Rev. B **79**, 195208 (2009)
- ⁹ Y. H. Choi, N. H. Jo, K. J. Lee, H. W. Lee, Y. H. Jo, J. Kajino, T. Takabatake, K.-T. Ko, J.-H. Park, and M. H. Jung, Appl. Phys. Lett. **101**, 152103 (2012).
- ¹⁰ Y.L. Chen et al, Science **329**, 659. (2010); K. Kuroda et al, Phys. Rev. Lett. **105**, 076802 (2010); I. Androulakis et al, Solid State Comm. **173**, 5 (2013)
- ¹¹ D. Parker and D. J. Singh, Phys. Rev. X **1**, 021005 (2011)
- ¹² A. Kokalj, J. Mol. Graph. Modelling **17**, 176 (1999).Code available from <http://www.xcrysden.org>.

-
- ¹³ D. Shoenberg, *Magnetic Oscillations in Metals* (Cambridge University Press, 1984)
- ¹⁴ V.R. Cooper, Phys. Rev. B **81**, 161104(R) , (2010)
- ¹⁵ P. Blaha, K. Schwarz, G. K. H. Madsen, D. Kvasnicka and J. Luitz, WIEN2k, An Augmented Plane Wave + Local Orbitals Program for Calculating Crystal Properties (Karlheinz Schwarz, Techn. Universitat Wien, Austria), 2001. ISBN 3-9501031-1-2.
- ¹⁶ J.P. Perdew, K. Burke and M. Ernzerhof, Phys. Rev. Lett. **77**, 3865 (1996).
- ¹⁷ P.M.C. Rourke and S.R. Julian, Comp. Phys. Comm. **183**, 324 (2012)
- ¹⁸ D. Parker and D.J. Singh, Phys. Rev. B **82**, 035204 (2010).
- ¹⁹ D.J. Singh, Func. Mat. Lett. **3**, 223 (2010).
- ²⁰ G.K. Madsen and D.J. Singh, Comput. Phys. Comm. **75**, 67 (2006).
- ²¹ S.K. Mishra, S. Satpathy and O. Jepsen, J. Phys.: Cond. Matt. **9**, 461 (1997).
- ²² H. Zhang, C-X. Liu, X-L. Qi, X. Dai, Z. Fang and S.-C. Zhang, Nature Physics **5**, 438, (2009).
- ²³ V.R. Cooper, Phys. Rev. B **81**, 161104(R) , (2010)
- ²⁴ P. Larson, V.A. Greanya, W.C. Tonjes, R. Liu, S.D. Mahanti and C.G. Olson, Phys. Rev. B **65**, 085108 (2002).



(a)



(b)

Fig 1.

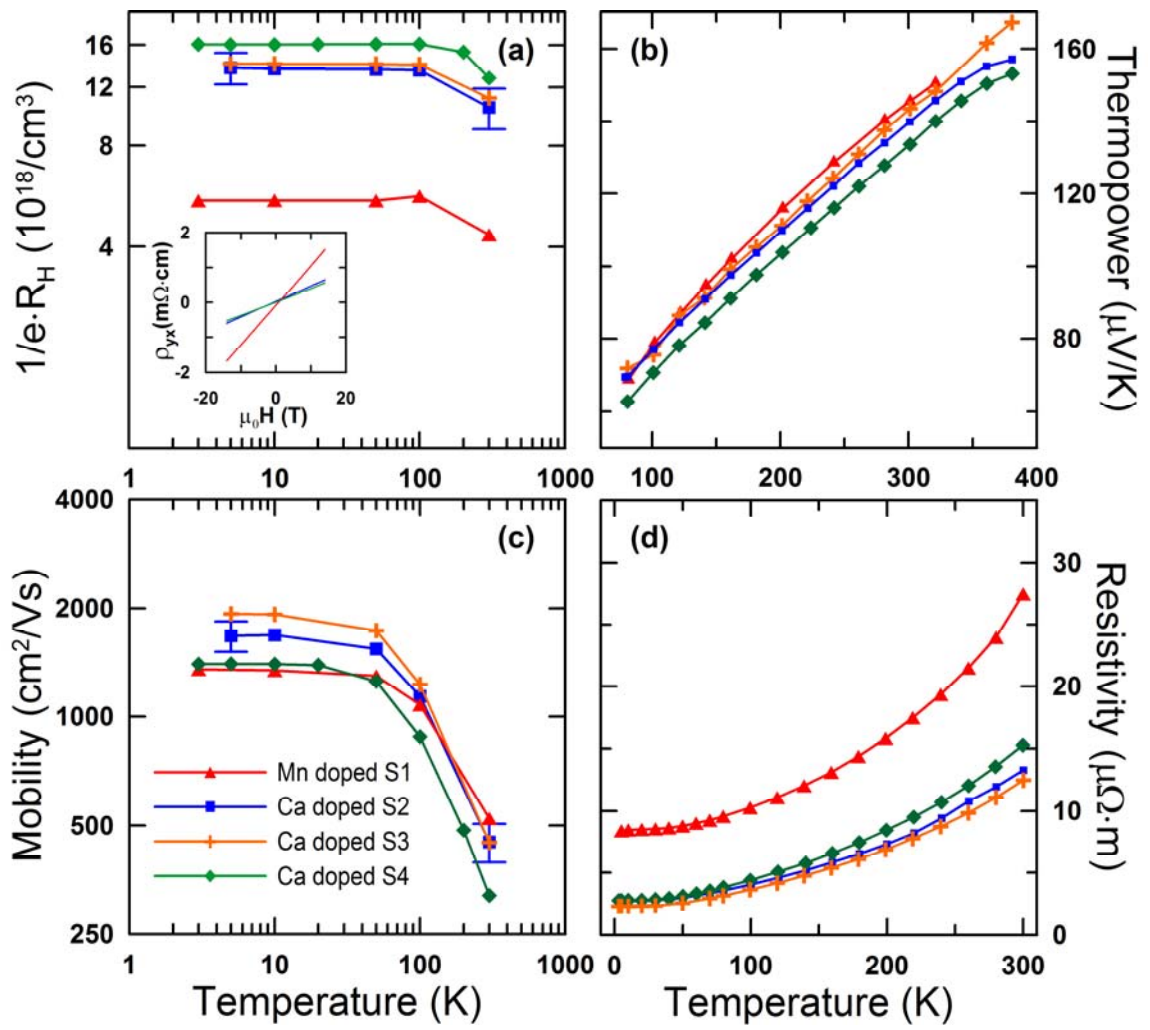


Fig 2.

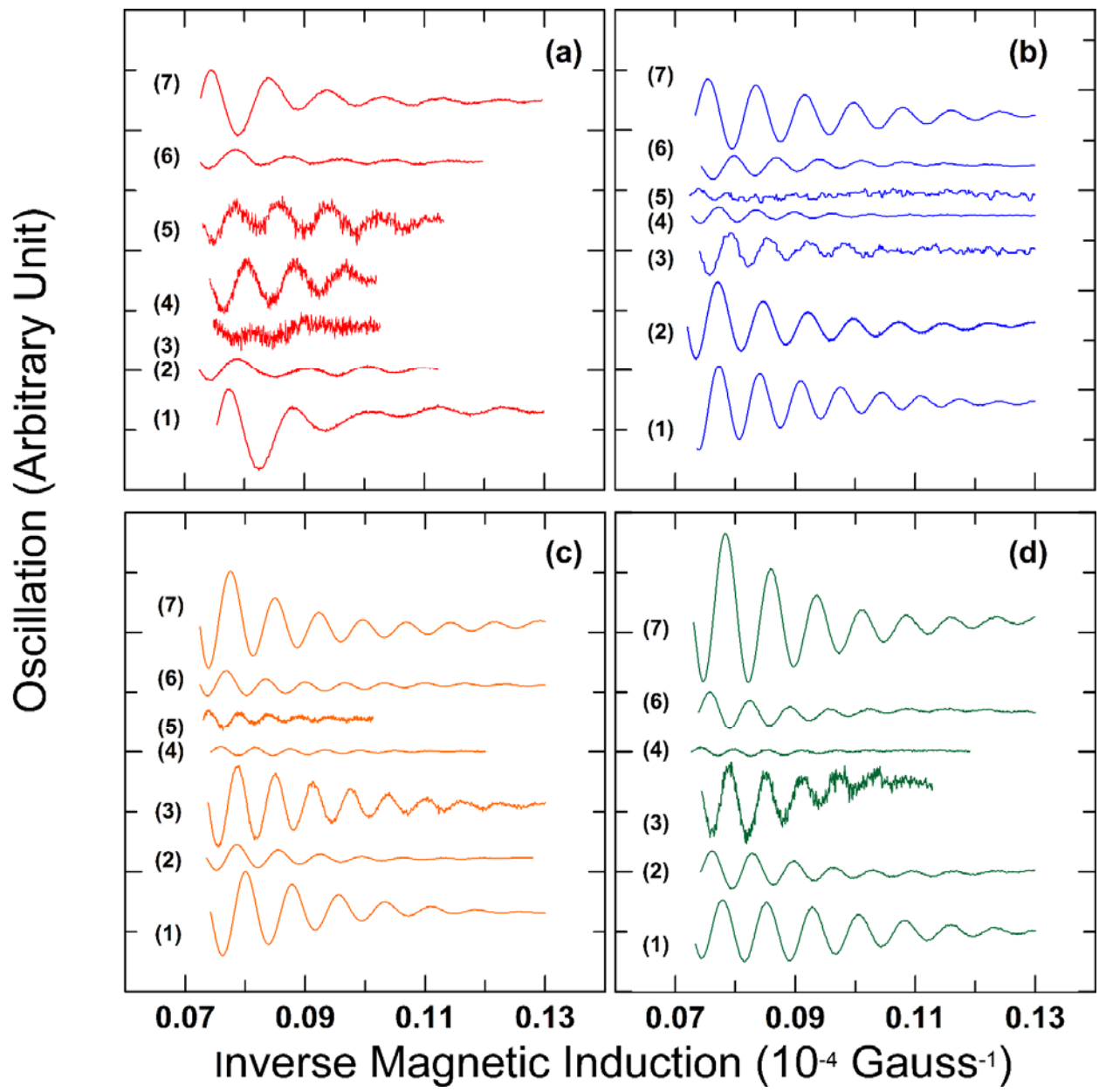


Fig 3.

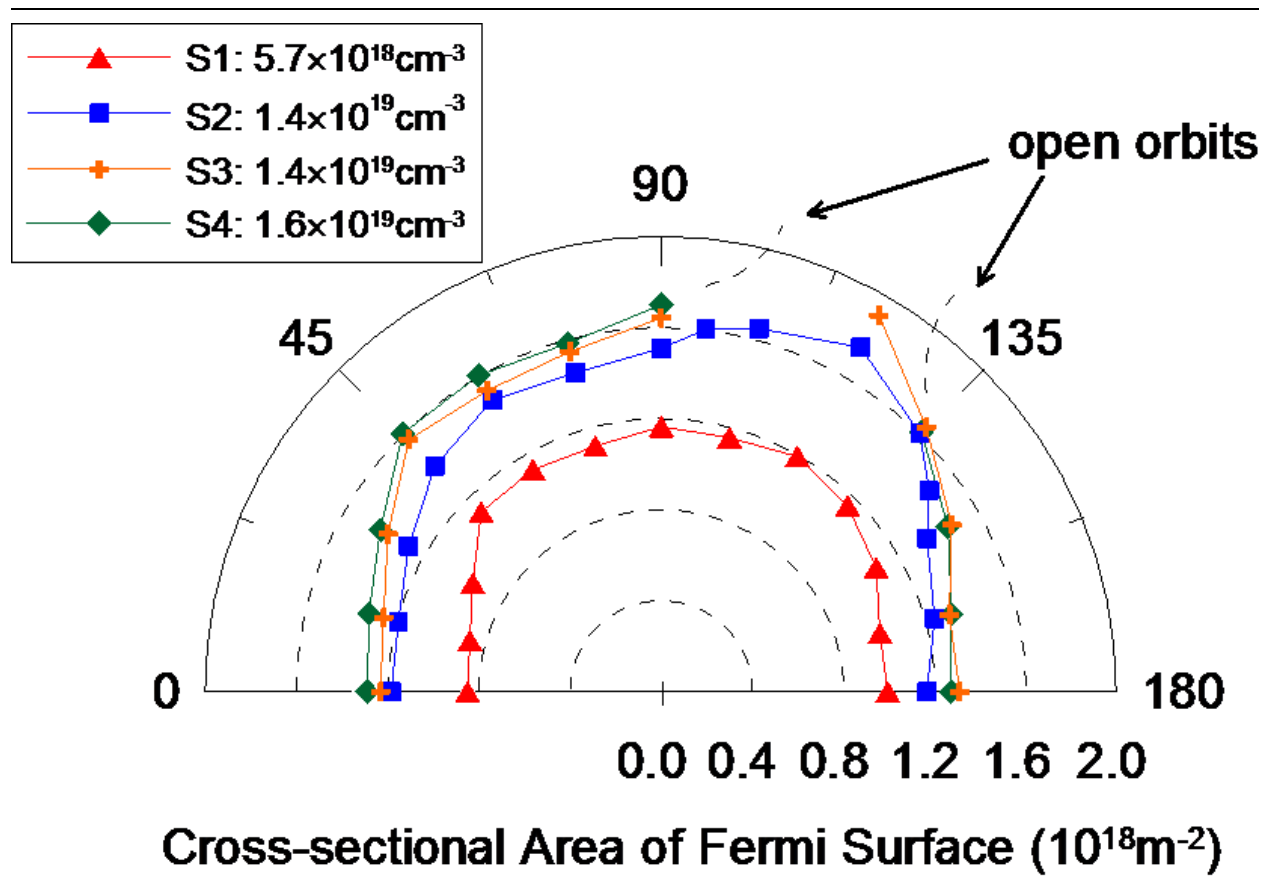


Fig. 4

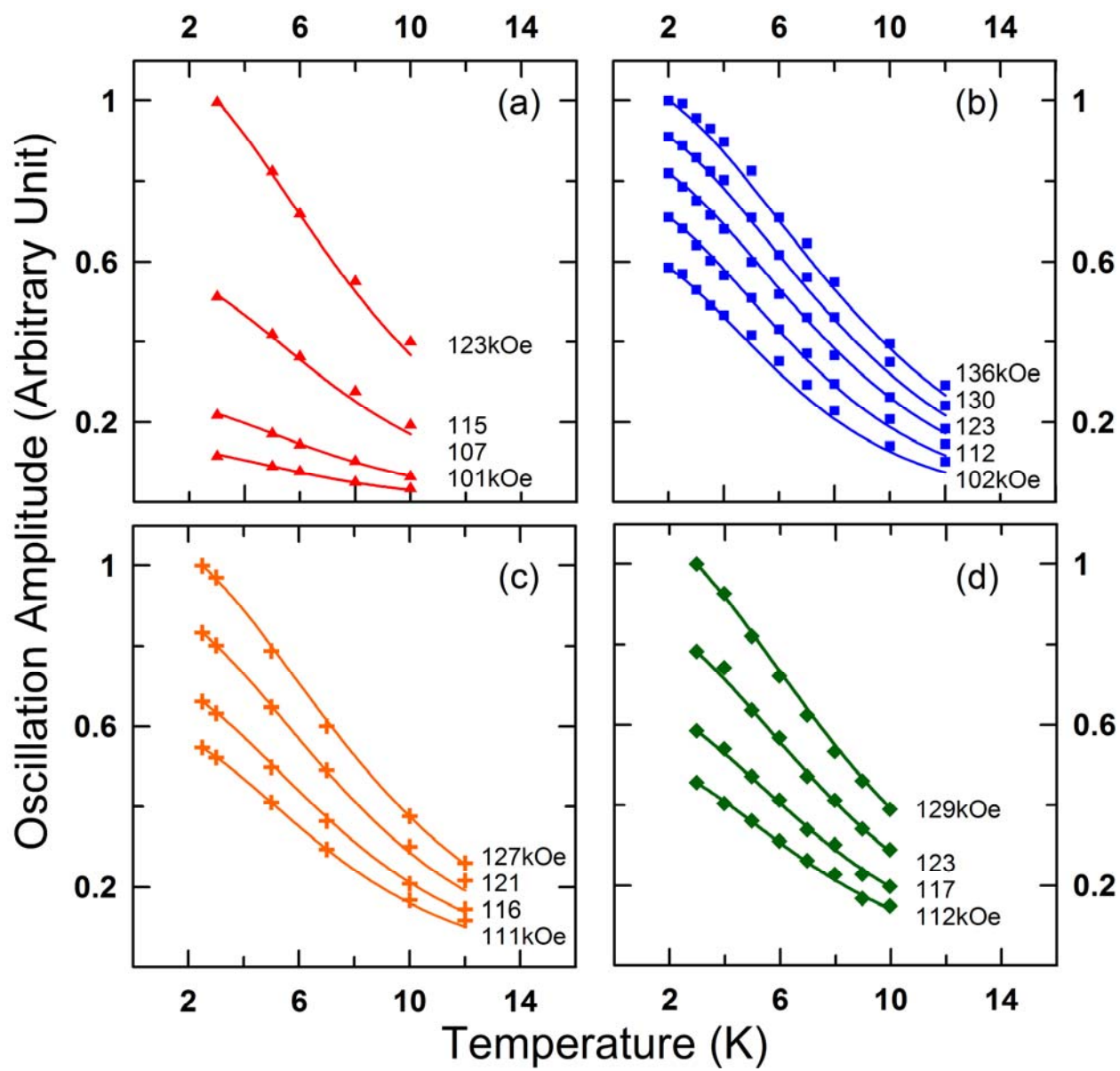


Fig. 5

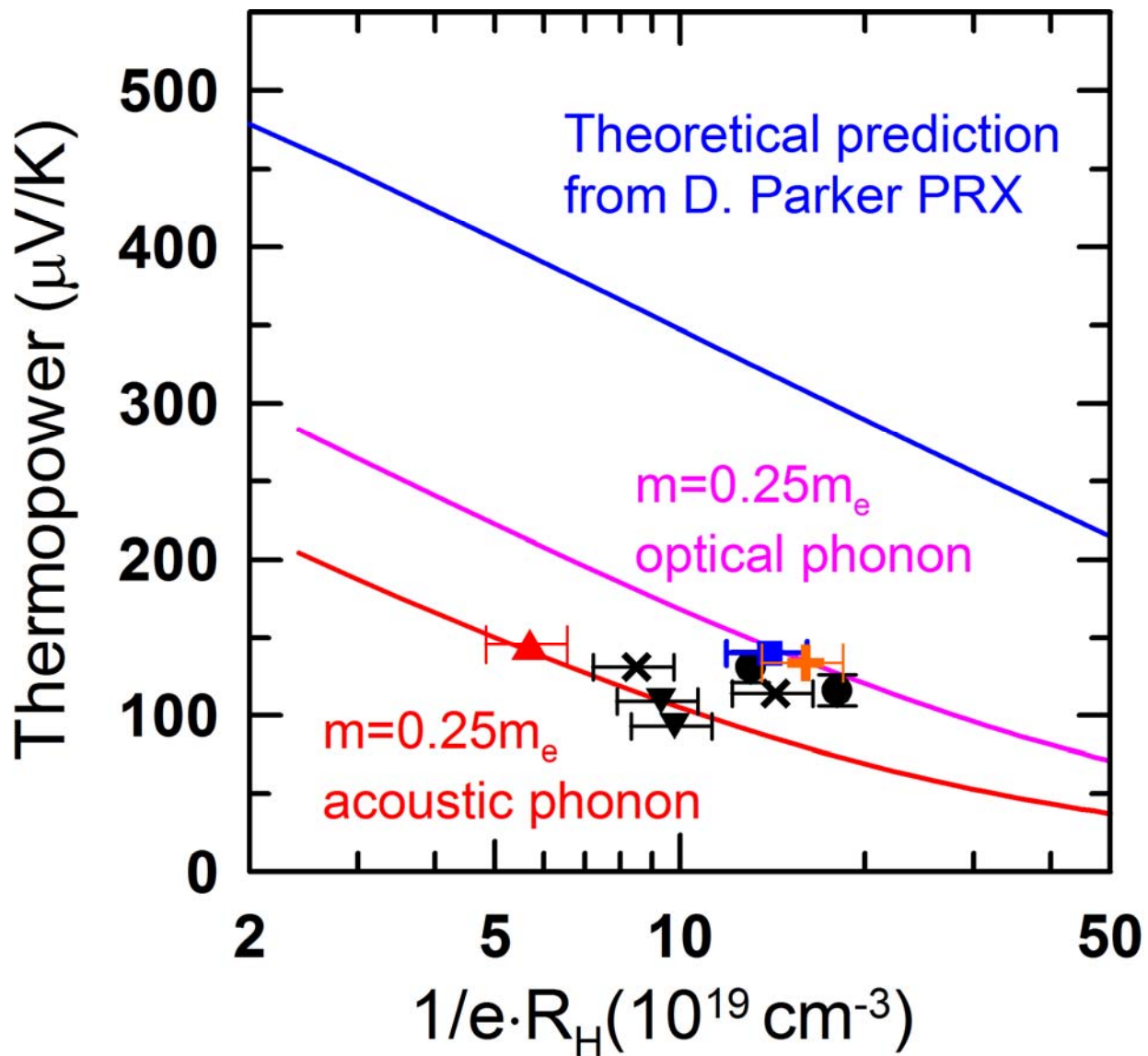


Fig. 6

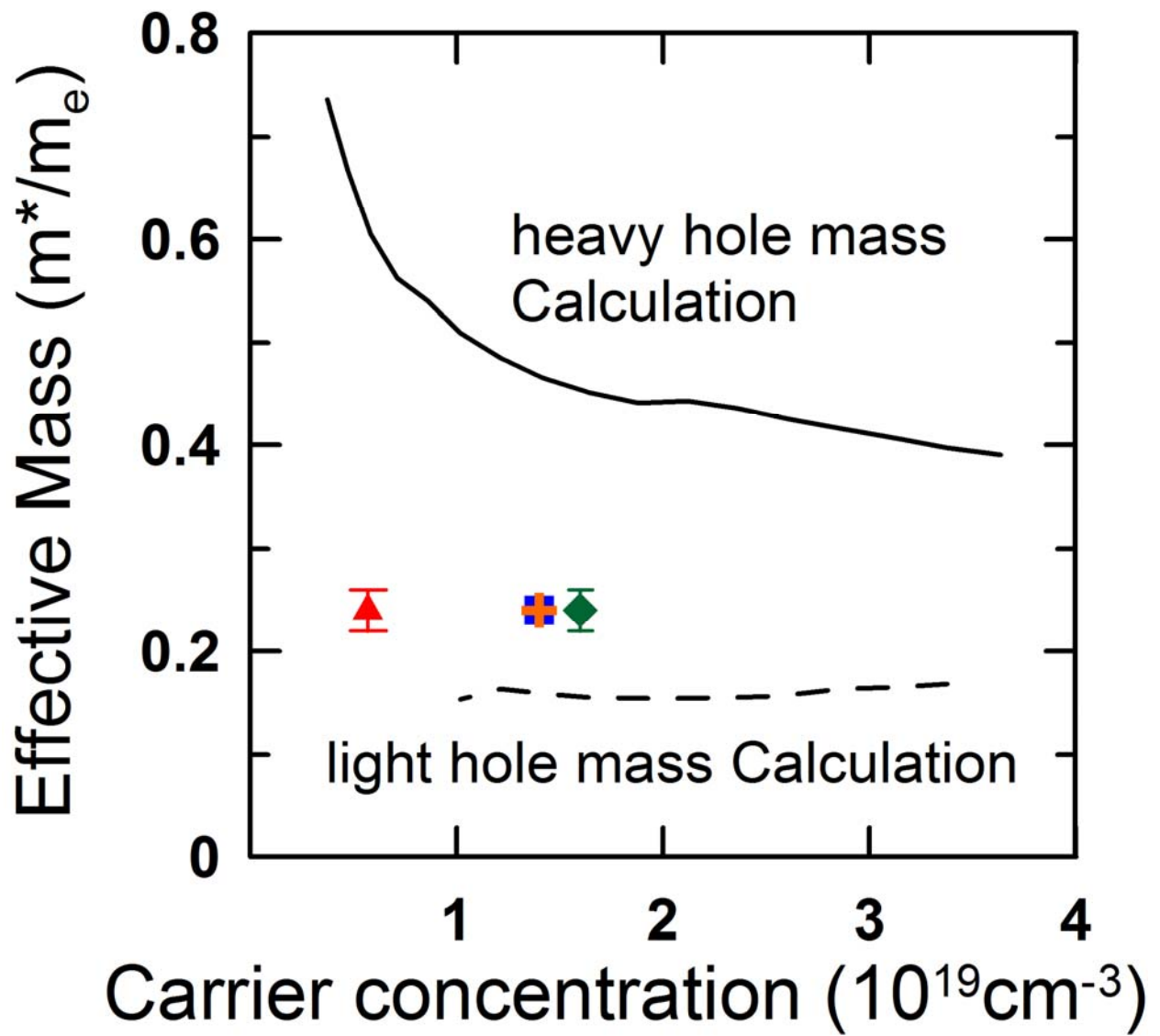


Fig 7